GEOPHYSICS, VOL. 89, NO. 2 (MARCH-APRIL 2024); P. E31–E45, 17 FIGS., 3 TABLES.
10.1190/GEO2022-0723.1

DOI:10.1190/geo2022-0723.1

Deep-learning-based airborne transient electromagnetic inversion providing the depth of investigation

Hyeonwoo Kang[1], Minkyu Bang[1], Soon Jee Seol[1], and Joongmoo Byun[1]

ABSTRACT

We develop an integrated workflow that uses deep-learning (DL)-based approaches for processing and inverting airborne transient electromagnetic (ATEM) data. Our novel workflow automates these preprocessing steps and enables real-time inversion in the field. Thus, we develop an entire inversion workflow using three DL networks that cover all steps from preprocessing to imaging. The preprocessing DL network performs interpolation to discard data that are severely noise contaminated and suppress the effects of noise in a late-time channel. We use an inversion DL network and a depth of investigation (DOI) network to generate images of subsurface resistivities exclusively within the DOI range where reliable predictions can be made. To optimize the inversion process, our approach focuses on designing the inversion DL network to simultaneously minimize data misfit and model misfit. By addressing these two aspects, we ensure a more robust outcome in the final resistivity images. The practical applicability of the workflow is verified by comparing the imaging results of the field data with those of conventional inversion and geologic interpretation. Each workflow is nearly automatic and very fast; we expect that our workflow will contribute to the development of real-time imaging software for the ATEM survey, which expands the applications of the ATEM survey in various fields.

INTRODUCTION

Airborne transient electromagnetic (ATEM) methods are commonly used for mineral exploration (Pfaffhuber et al., 2009; Yang and Oldenburg, 2013; Kang et al., 2017; Law et al., 2019), hydrogeologic investigation (Smith et al., 2004), and site characterization (Dethlefsen et al., 2013) because they rapidly map subsurface conductivity variations over large areas. However, as the data volume typically consists of one million data points or more, efficient inversion is essential when interpreting an entire data set. Therefore, to achieve meaningful insights from the data, it is crucial to have a workflow that can handle such a large volume of data efficiently. To accurately image real subsurface structures exhibiting 2D and 3D conductivity variation, 2D and 3D inversion methods are required, respectively. Guillemoteau et al. (2012) develop an empirical 2D inversion method incorporating an approximation of the "Frechet kernel" and Cox et al. (2010) use a moving footprint approach that accelerates computation and increases efficiency by inverting many relatively small areas instead of the entire 3D area. However, 2D and 3D inversion of entire ATEM data sets remain challenging; the computational demands (time and memory) are very high and the appropriate parameter settings change according to the condition of the data. Thus, historically, ATEM data have often been interpreted using 1D methods, such as imaging methods (Liu and Asten, 1993; Tartaras et al., 2000; Christensen, 2002; Huang and Rudd, 2008) and constrained inversion (Auken et al., 2005; Viezzoli et al., 2008; Hauser et al., 2015).

Although 1D inversion is very fast compared with 2D and 3D inversion, it is still very time consuming to invert a vast amount of data collected over large areas. Given the recent rapid growth of deep-learning (DL) technology, several attempts have been made to achieve DL-based inversion of ATEM data, which would accelerate and generalize the inversion problem. Feng et al. (2020) construct a simple neural network with only two hidden layers that predicts the all-time apparent resistivities, rather than inverted subsurface resistivities, using time constants, the amplitudes of induced voltages, and altitudes as inputs. Bai et al. (2020) develop an artificial neural network inversion method using the ATEM responses and several time gates as input and the output is the inverted resistivities. Li et al. (2020, 2021) use DL technology to replace the earlier simple neural networks used for ATEM inversion. Recently, a convolutional neural network (CNN) and a recurrent neural network

Manuscript received by the Editor 1 December 2022; revised manuscript received 10 November 2023; published ahead of production 21 November 2023; published online 30 January 2024.
[1]Hanyang University, Department of Earth Resources and Environmental Engineering, Seoul, South Korea. E-mail: hykanghw@gmail.com; wbmaicon13@gmail.com; ssjdoolly@hanyang.ac.kr (corresponding author); jbyun@hanyang.ac.kr.

have been used for ATEM inversion (Puzyrev and Swidinsky, 2021; Wu et al., 2021a, 2022). These networks extract latent mapping relationships with high efficiency and reduce computation costs by sharing parameters. Currently, these techniques yield inversion results for real field data that are comparable with those of conventional methods (Wu et al., 2022).

Apart from field data inversion, interpretation of ATEM data requires a reliable depth range for the inversion results, which is known as the depth of investigation (DOI). As a conductive layer prevents current diffusion downward, transient sounding methods cannot deliver layer information below a conductive medium. In other words, conductivity variations below a certain depth are not detected at the receiver, so we cannot have confidence in the conductivity values below the DOI. Thus, many researchers have sought to provide the DOI and inversion result using conventional approaches. For example, Spies (1989) uses an approximation equation to predict the DOI, and Christiansen and Auken (2010) determine the DOI by calculating the cumulative sensitivity.

It is also essential to reduce the effect of noise. As voltage responses are often disturbed by the motions of vehicles (e.g., roll, pitch, and yaw) and electromagnetic coupling with infrastructure (pipes, fences, power lines, and telephone cables), voltage amplitude often oscillates, especially at late times (because the amplitude decreases over time) (Wu et al., 2021b; Asif et al., 2022). Thus, appropriate data selection and thorough denoising are always required for the successful interpretation of ATEM data (Auken et al., 2009; Kang et al., 2021). Recently, to enhance processing efficiency, DL techniques have been used to denoise transient electromagnetic (TEM) data (Wu et al., 2021b; Asif et al., 2022; Chen et al., 2022).

In the field of ATEM geophysical surveys, preprocessing, DOI estimation, and inversion techniques play a crucial role in extracting meaningful information from the collected data. However, conventional approaches use a sequential process including manual preprocessing, inversion, and DOI estimation, which is not only time consuming but also challenges reproducibility. Thus, we introduce an integrated inversion workflow that not only inverts ATEM data but also performs preprocessing and calculates the DOI. We use three different DL-based networks to this end. CNN models are used for the interpolation of field data and the inversion of the interpolated data. A simple DL network is used to predict the apparent resistivity (ρ_a) required when calculating the DOI. We validate the workflow by applying it to field data already interpreted by Bedrosian et al. (2014) and Wu et al. (2022). As our workflow rapidly covers the steps from preprocessing to imaging in a near-automatic way, it greatly aids the interpretation of a vast amount of field data.

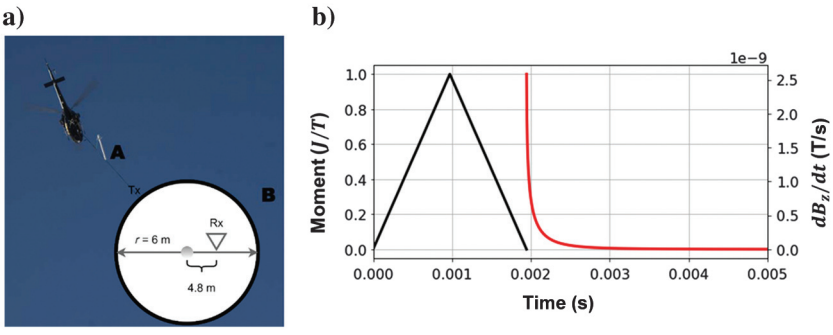

Figure 1. (a) Schematic representation of the AeroTEM IV system (USGS, 2011). A is the magnetometer bird and B is the AeroTEM IV bird. (b) An example of the current waveform and TEM responses recorded by the receiver. The solid black and red lines indicate the waveform and voltage responses, respectively.

DATA PREPARATION

Composing a high-quality training data set that covers all field data characteristics is essential for training a DL-based inversion network. Thus, the characteristics of the target data are first analyzed, and a training data set that includes all of the characteristics is generated. In this section, we introduce the field data and survey geometries and then describe how to construct a training data set that simplifies the characteristics of the target data.

Target data analysis

Our target data are obtained in an exploration conducted by the United States Geological Survey (USGS) that aimed to understand and manage groundwater resources in the arid environment of the Leach Lake Basin (Fort Irwin, CA, USA). We select these data because they have been interpreted using various methods, such as conventional inversion (Bedrosian et al., 2014) and DL-based inversion (Wu et al., 2022). We consider that the use of these data would aid the verification of our results. ATEM data have been obtained using the AeroTEM IV system (Aeroquest Ltd., Mississauga, Canada). As shown in Figure 1a, this system has a transmitter loop 12 m in diameter and a horizontal coplanar (HCP) system in which a receiving coil is located behind the center of the transmitter at an elevation of 4.8 m. This system repeatedly transmits a symmetric triangular current pulse for 1.945 ms, stops, and measures the secondary field caused by the eddy current induced on the subsurface (in the shape of a smoke ring); the ring diffuses downward as time passes (Figure 1b). The raw streaming data are sampled at 36 kHz, prefiltered with a three-point filter, stacked using a boxcar stacking algorithm, and binned to 17 off-time channels from 2.14 to 4.71 ms in Figure 1b. This range corresponds to a time range of 0.195–2.765 ms after the transmitter is turned off, as reported in the AeroTEM report (USGS, 2011).

Analysis of the laser altimeter data confirms that most data were obtained between 20 and 80 m (Figure 2a). Data measured at altitudes of >80 m cannot be interpreted because the sensitivity is too low (Figure 2c). Data measured at altitudes of <20 m are easily affected by topographic changes and errors in the survey geometry. Thus, we interpret only field data obtained at altitudes of 20 and 80 m.

As shown in Figure 3, ATEM data are measured along flightlines totaling 1,700 line km within a 46 km × 16 km survey block. Most flightlines are oriented north–south; the three tie lines are oriented east–west and run along the northern and southern boundaries and through the center of the survey block (Bedrosian et al., 2014). Excluding the tie lines, the number of flightlines is 101. The spacing between the survey lines for approximately 70% of the block is approximately 400 m and that for the rest of the block (in the east) is approximately 800 m (Figure 3).

Construction of 1D resistivity models

To successfully train a DL model, a large amount of training data for various resistivity models that accurately reflect the characteristics of the target

field data is required. To properly interpret multidimensional (2D or 3D) ATEM data, training data should be generated on 2D or 3D subsurface structures having horizontal conductivity variations. However, it is important to note that when dealing with 2D or 3D subsurface structures, the number of potential model parameters becomes exceedingly large, encompassing factors such as the quantity, positions, and shapes of conductive anomalies as well as background conductivity variations (Bang et al., 2022). Thus, most DL-based inversions have conducted 1D interpretations (Bai et al., 2020; Feng et al., 2020; Li et al., 2020; Puzyrev and Swidinsky, 2021; Wu et al., 2022).

Fortunately, AeroTEM IV data are amenable to 1D interpretation because this HCP system exhibits only a small offset. Therefore, we choose a 1D interpretation approach that has a great advantage in constructing extensive training data sets while reducing computational time.

To train the 1D inversion network, 1D resistivity models representing various underground structures are systematically generated using the following rules. First, we use a maximum resistivity model depth of 500 m because previous inversions have depths of 300–600 m (Hutchinson et al., 2010; Bai et al., 2020; Madsen et al., 2022; Wu et al., 2022). Second, given that data sensitivity decreases as the depth increases, we divide the 500 m into 13 layers over which the thickness increases on a logarithmic scale. Third, up to three different boundaries are randomly selected from 12-layer boundaries and resistivities, which are divided equally using a logarithmic scale from 1 to 1000 ohm-m, and systematically applied to the layers between the selected boundaries. We generate 99,570 resistivity models including 30 half-space models, 2520 two-layer models, and 97,020 three-layer models. We limit the training data to three-layer models because including models with more than three layers significantly increases the degrees of freedom, leading to extended training times and potentially increasing the nonuniqueness problem in 1D inversion. If nonuniqueness is not adequately controlled, it may even hinder the efficiency of the training process. The target data indicate that ATEM responses are required for altitudes of 20–80 m for each resistivity model. Given the effect of altitude on sensitivity, we decide to perform numerical simulations at 5 m intervals of 20–50 m and 10 m intervals at higher altitudes.

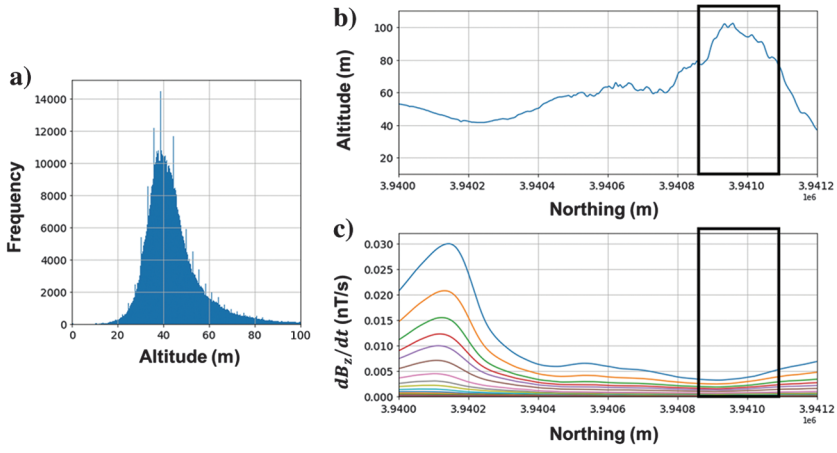

Figure 2. (a) Altitude distribution measured by the laser altimeter, (b) altitude range, and (c) voltage responses along the 10,540 line. The areas marked with the solid black rectangles in (b) and (c) are areas of >80 m and the responses of those areas, respectively.

Depth of investigation

Electromagnetic methods have limitations when it comes to accurately evaluating the layers located beneath a conductive medium. Specifically, when using the transient sounding technique, the current tends to stay within the conductive medium, even during the late-time phase of measurement. As a result, a low-resistivity layer can obstruct the current diffusion pattern and act as a shield for the high-resistivity layer located beneath it (Kirsch, 2009). Consequently, even if there is a change in resistivity in a layer located beneath a conductive layer, this change may not be evident in the voltage response over the measurement time range.

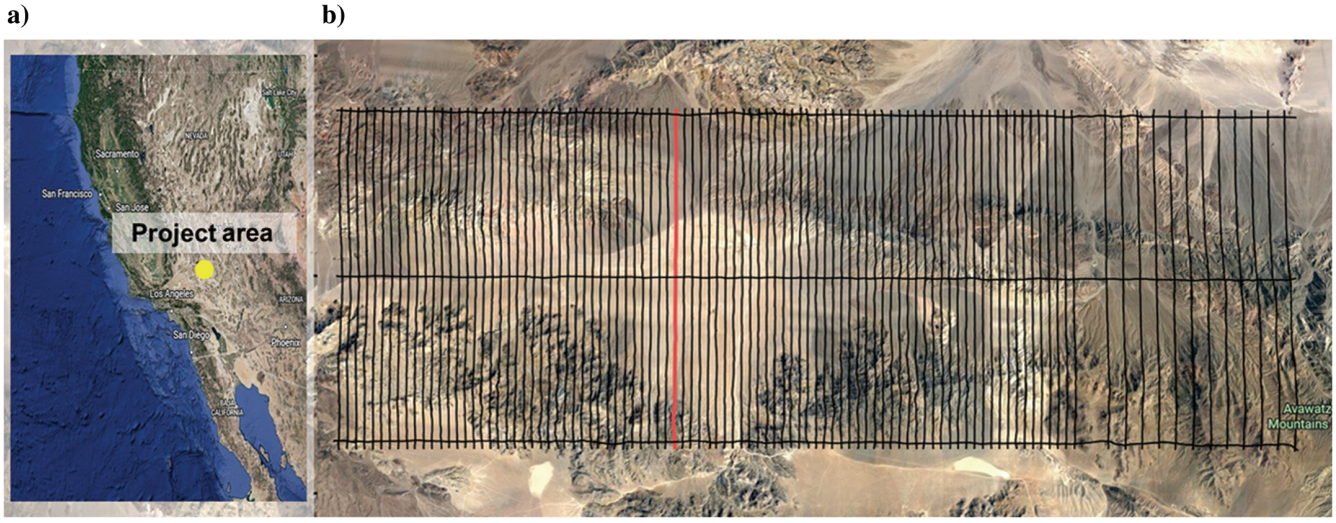

Figure 3. The location of Fort Irwin, California (the yellow circle in [a]) and (b) the flight path (Google Earth, 2014).

To overcome this issue, geologists and geophysicists have defined a DOI, which has been the subject of numerous studies. Some notable works include the Spies (1989) late-time approximation method and the Christiansen and Auken (2010) cumulative sensitivity method. In our study, we use Spies' method because the DOI can be easily evaluated by calculating the noise level of the field data and the apparent resistivity of the inverted resistivity model.

There are no generalized analytic solutions for various transmitter and receiver geometries. However, in a homogeneous half-space, an analytic solution exists for the "in-loop configuration," and the voltage response at late time (t_L) is

$$\eta_v = \frac{I\mu_0^{2.5}a^2}{20\sqrt{\pi}} \cdot {\rho_a}^{-1.5} \cdot t_L^{-2.5}, \tag{1}$$

as described by Spies (1989) because late-time voltage response (η_v) can be linearly approximated in the logarithmic domain, proportional to $t^{-2.5}$. In equation 1, I is the current, μ_0 is the magnetic permeability, a is the loop radius, and ρ_a is the apparent resistivity.

Noise is generally an unnecessary signal other than the desired signal, and field data cannot be used when the amplitude of the signal becomes smaller than that of the background noise. Therefore, the noise level can serve as a criterion for the measurable late-time voltage response and provide information on the penetration depth, i.e., the diffusion depth (δ_{TD}). The diffusion depth corresponding to the late time can be calculated using the following equation (Ward and Hohmann, 1988):

$$\delta_{TD} = \sqrt{\frac{2t_L}{\mu_0} \cdot \rho_a}. \tag{2}$$

The DOI then can be determined by combining the late-time approximation and diffusion depth (Spies, 1989):

$$\mathrm{DOI} = 0.55\left(\frac{IA}{\eta_v}\rho_a\right)^{\frac{1}{5}}, \tag{3}$$

where A is the area of the loop.

To check the applicability of this equation to our ATEM configuration rather than the in-loop configuration, late-time voltage responses of the ATEM configuration for homogeneous half-spaces are numerically calculated and compared with those of the in-loop configuration, as shown in Figure 4a. Although the late-time response is not proportional to $t^{-2.5}$, as shown in Figure 4a, it also appears to be linearly approximated in the logarithmic domain. Thus, we modify the late-time approximation equation as follows:

$$\eta_{\mathrm{mod}} = \alpha\frac{I\mu_0^{2.5}a^2}{20\sqrt{\pi}} \cdot {\rho_a}^{-1.5} \cdot t_L^{\beta}, \tag{4}$$

where α is the static shift and β is the slope of a late-time linear equation. For the AeroTEM IV system, we find that the α and β values are 0.01 and -3, respectively, and Figure 4b shows that the approximation fits the late-time voltage responses well. As a result, we propose

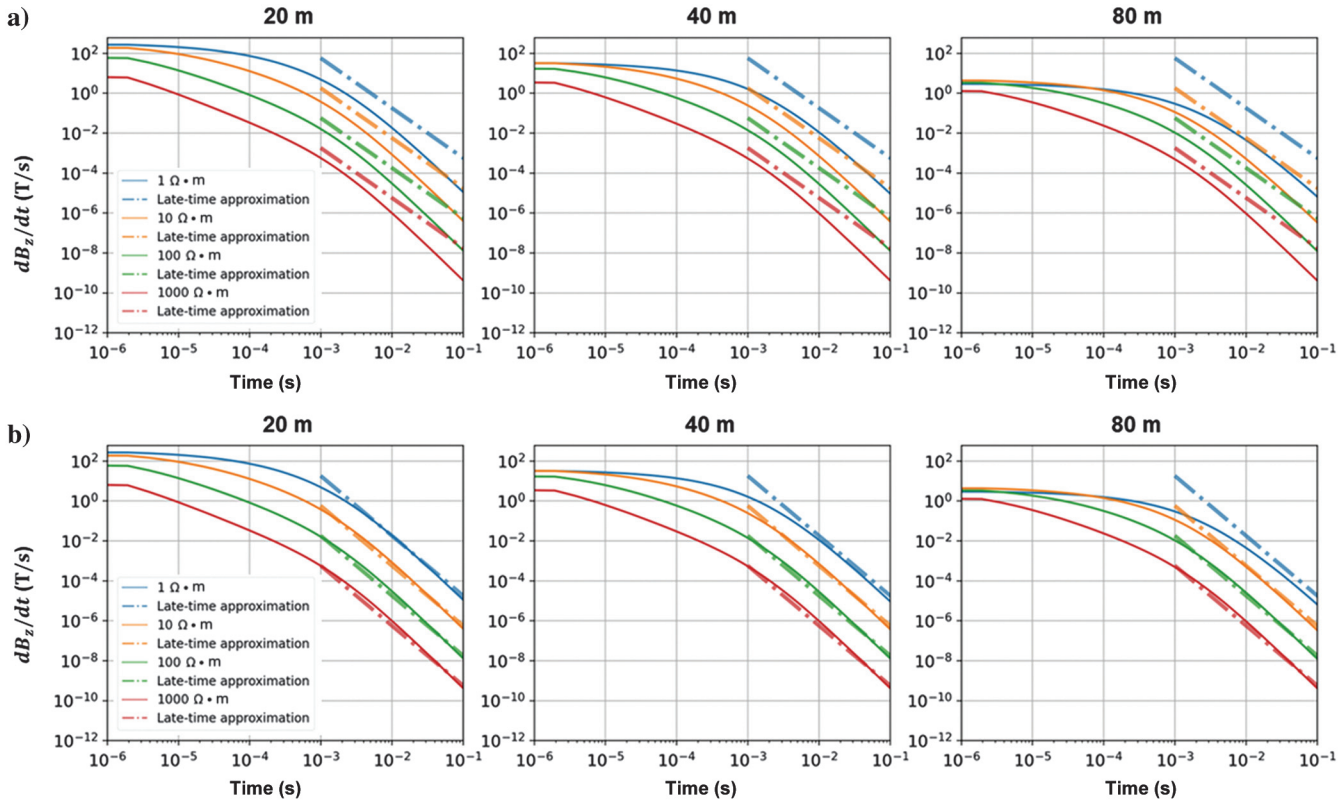

Figure 4. Comparison of the numerical modeling results and late-time approximations for transmitter-receiver models at altitudes of 20, 40, and 80 m, corresponding to electrical resistances of 1, 10, 100, and 1000 ohm. (a) Corresponding to the original approximation equation and (b) comparison with the modified equation.

the modified DOI equation for the AeroTEM IV system by combining the modified equation and diffusion depth as follows:

$$\mathrm{DOI} = 0.928\left(\frac{IA}{\eta_{\mathrm{mod}}}\rho_a^{1.5}\right)^{0.167}. \tag{5}$$

DL NETWORKS

In this section, we describe the three different neural networks used. The first DL network is a preprocessing network that reduces the effects of noise by interpolating the 16-channel field data to 63 points. In fact, the field data are measured using 17 off-time channels. However, as the first-channel values of most TEM responses show more obvious static shifts than those of the other channels, only the 16-channel data are used for interpretation; the first-channel data are excluded. The second DL network inverts the TEM responses to layer resistivities. The third (simple) neural network is the DOI network, which estimates the apparent resistivities from the TEM responses for calculating the DOI.

Preprocessing network: Noise reduction and interpolation

In general, early time TEM responses yield shallower geologic information, whereas late-time responses provide deeper information. However, late-time responses tend to be contaminated with coherent electrical or background noise because the amplitudes are 10^2 or 10^3 times smaller than those of early time amplitude. As shown in Figure 5, the values of some data are sufficiently large to overcome any effect of noise (Figure 5a), but many data were severely noise contaminated, especially in late time (Figure 5b). Because these data can lead to misinterpretations, Auken et al. (2009) address the necessity of preprocessing to ensure the preservation of data quality, such as flight altitude, tilt of transmitter frame, and the removal of coupling caused by man-made structures. To mitigate any flaws or misinterpretations that may arise, we use a data screening method and a preprocessing approach based on DL techniques to effectively remove the coupled noise from the data.

Scaling method

In general, TEM responses are evaluated using a logarithmic scale because the amplitude decay decreases exponentially. However, this general scale can exaggerate very small variations at late times, such as sign changes or oscillations. In addition, it cannot directly handle the negative TEM responses resulting from capacitive coupling, such as induced polarization effects (Weidelt, 1982; Kang and Oldenburg, 2016). To address this issue, we introduce a logarithmic scaler that has been shifted by a small value, denoted as "epsilon (ε)," along the x-direction. By implementing this approach, we effectively reduce the amplification of small variations that may occur with a general logarithmic scale.

In the field of DL, scaling techniques are commonly used to preprocess the input data. The main reason to use scalers (e.g., standard scaler, robust scaler, and min-max scaler) is to bring all the features or variables to a similar scale or range to enhance the efficiency of training. In equation 6, when ε is equal to zero, this can be called the "min-max scaler," which transforms the data values to a range between 0 and 1 while preserving the relationships between the data points. In our case, we use a modified min-max scaler with a logarithmic scaled value shifted by $-\varepsilon$:

$$\frac{\log_{10}(X+\varepsilon) - \log_{10}(X_{\mathrm{min}}+\varepsilon)}{\log_{10}(X_{\mathrm{max}}+\varepsilon) - \log_{10}(X_{\mathrm{min}}+\varepsilon)}, \tag{6}$$

where X_{min} and X_{max} are the minimum and maximum TEM responses, respectively. Using this modified transformation, noise that is boosted in late-time channels in ordinary min-max transformation using logarithmic scaled data (Figure 5b) is sufficiently suppressed (Figure 5d). The absolute value ($-\varepsilon$) should be chosen to reflect the characteristics of the target field data and should be greater than the absolute minimum negative value of all field data.

Interpolation network structure and training method

In Figure 6, the interpolation network consists of an encoder and decoder structure that contracts and expands features from the input data. The encoder uses two convolutional layers followed by max pooling layers to progressively reduce the spatial dimensions of the input data. Meanwhile, the decoder uses two convolutional layers followed by upsampling layers to gradually increase the dimensions of the data. The output from the expanding path is combined with the corresponding feature map from the contracting path through concatenation. This approach allows the network to recover fine-grained details that may have been lost during the contraction process, which is particularly useful for interpolation tasks. The number of input and output nodes is set to 16 and 24, respectively. We make this decision because each max pooling layer in the encoder and

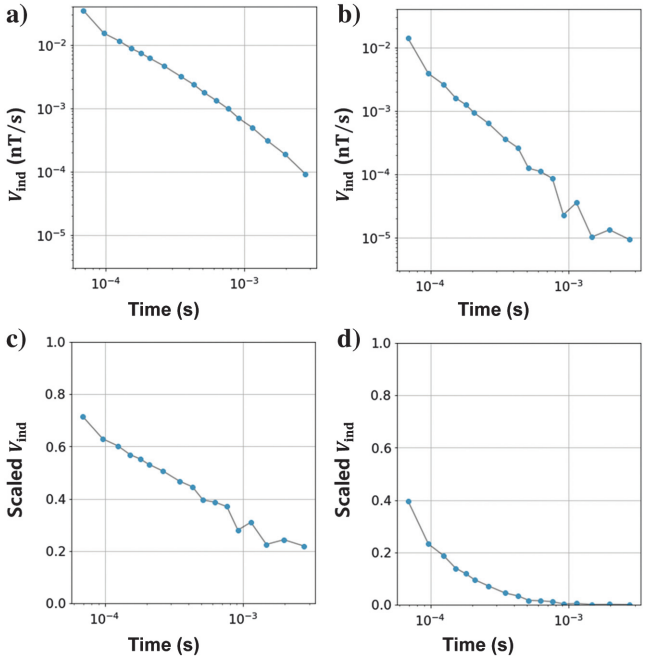

Figure 5. Example of field data. (a) Clean data with minimal noise and (b) noisy data; noise contamination is especially severe in the late-time channels. The first-time channels for both data sets are obviously more extensively shifted than the other channels. (c) Min-max scaled data of (b) after application of the ordinary logarithmic transformation. (d) Min-max scaled data of (b) after application of the shifted logarithmic transformation.

each upsampling layer in the decoder decreases or increases the spatial dimensions of the input data by a factor of two. Consequently, we start with 16 input nodes and gradually decrease the number of nodes in subsequent layers while increasing them in the decoder. The detailed hyperparameters are provided in Table 1.

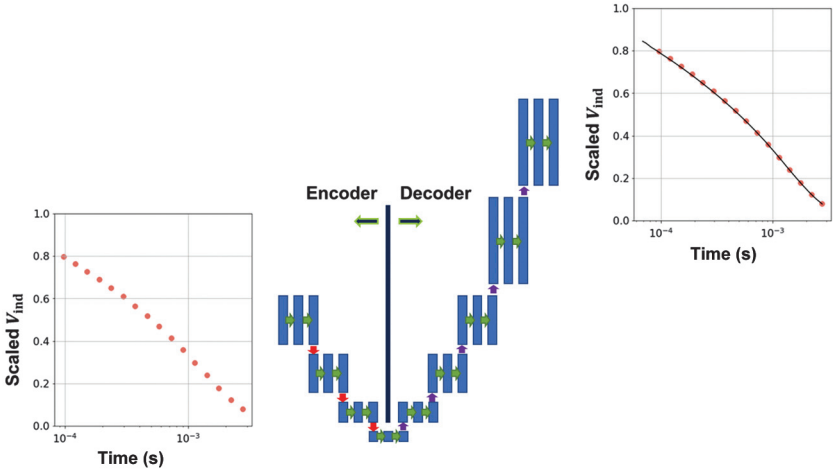

Figure 6. A schematic representation of the interpolation network. The red dots in the input and output images represent the scaled data. The solid black line in the output indicates the interpolated results.

Table 1. Detailed architecture of interpolation network.

Contracting		Expanding	
Layers	Output dimension (output, channel)	Layers	Output dimension (output, channel)
Input	(16,1)	Fifth layer	(4,256)
First layer	(8,64)	Sixth layer	(8,128)
Second layer	(4,128)	Seventh layer	(16,64)
Third layer	(2,256)	Eighth layer	(32,32)
Fourth layer	(2,512)	Ninth layer	(64,1)

To train the network, we calculate the voltage responses at 63 sampling times of 99,570 resistivity models at 10 different altitudes and we make the downsampled pair of each voltage response. We downsample the 63 computed samples to 16 samples because the raw data consist of 16 data samples. The 63 data samples are used as labels and the 16 data samples are used as input for training the interpolation network. In addition, to enhance the network's ability to handle the noisy field data, we create two supplementary training data sets. These data sets incorporate two distinct sets of Gaussian-distributed noise, each with a minimum and maximum value of $\pm 2.27 \times 10^{-5}$ nT/s, into the input data, as shown in Figure 7. Thus, a total of 2,987,100 ($99{,}570 \times 10 \times 3$) training data sets have been established, with the noise-free data sets also acting as labels for the noisy input data sets. We successfully interpolate field data that are varied in terms of amplitude, decay pattern, and noise (Figure 8). The interpolated and scaled voltage responses with 63 samples are combined with the min-max scaled altitude and the combined 64 datapoints are used for the inputs of the next inversion and DOI networks.

Noisy data screening

Data obtained from ATEM measurements can be disturbed by different types of noise, such as sudden changes in vehicle speed or altitude, and capacitive couplings. Although filtering is commonly used to remove such noise, data screening is also crucial to ensure that the quality of the uncoupled data is not degraded. Auken et al. (2009) emphasize the importance of manual processing to remove culled data, whereas more recently,

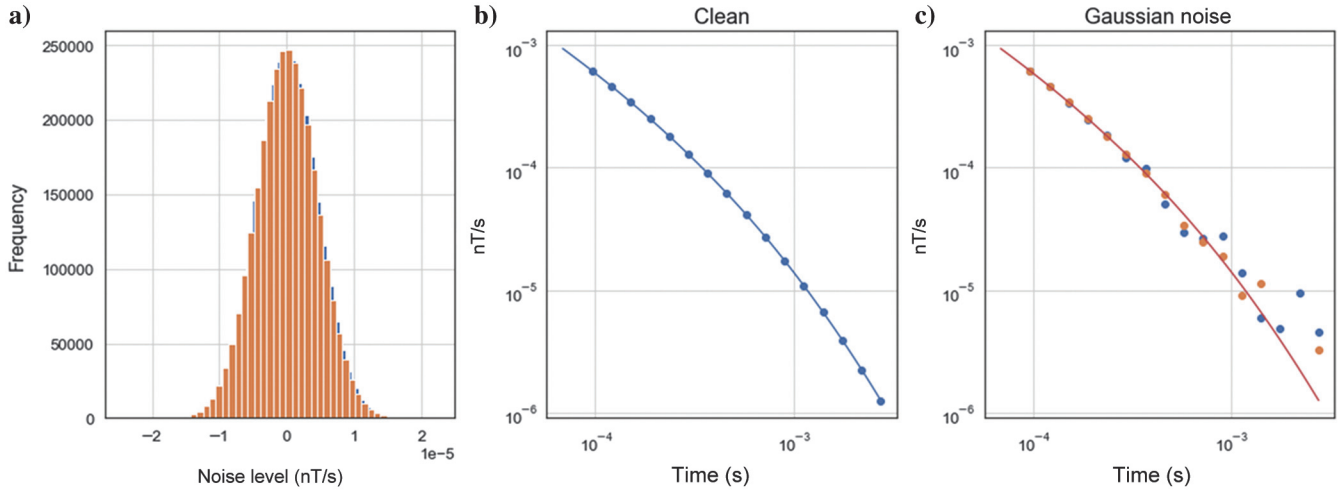

Figure 7. (a) The Gaussian-distribution noise to add to clean data, (b) the original data, and (c) the original data (the red line) and noise-added data sets (the blue dots and orange dots).

Asif et al. (2022) develop a DL-based expert system that uses a specific metric to filter out bad data while preserving the quality of the uncoupled data.

In this study, to obtain more reliable predictions of field data, we have incorporated a data screening process into our workflow. Specifically, we use an interpolation network to remove noise in advance and then compute the Euclidean distance between the preprocessed and field data to evaluate the quality of field data using the following equation:

$$D(d_{\text{intp}}, d_{\text{field}}) = \sqrt{\sum |d_{\text{intp}} - d_{\text{field}}|^2}, \tag{7}$$

where d_{intp} is the interpolated data and d_{field} is the raw data measured in 16 channels. By implementing this screening step, we can remove bad input data in advance, which can be a major cause of unreliable prediction.

Figure 9a shows the distribution of Euclidean distances in our field data. Within this distribution, approximately 85% of the data points fall within the range of 0–0.01. This range corresponds to a Z-score of one from the left side, which is calculated using

$$Z = \frac{X - \mu}{\sigma}, \tag{8}$$

where X is the value being evaluated, μ is the mean value of X, and σ is the standard deviation of X. To ensure a normal distribution, we apply a logarithmic transformation to the distances due to the observed skewness in their distribution. This transformation yields a distribution suitable for calculating the Z-scores.

Notably, the data points falling within the range of 0–0.01 exhibit high quality, enabling reliable denoising and interpolation, as shown in Figure 9b. Consequently, we make the decision to use the data enclosed within the solid black box. Conversely, Figure 9c shows that when Euclidean distances exceed 0.01, the raw data remain severely contaminated with noise, even with the use of a shifted logarithmic scale.

Inversion network

ATEM inversion is a process that uses the relationship between the attenuation pattern of voltage response and the resistivity model. Traditional DL-based inversion networks have limitations in guaranteeing data misfit, leading to the development of physics-informed inversion by Colombo et al. (2021). This research performs an efficient DL-aided inversion by combining the advantage of the DL network with the conventional inversion method. However, it still requires an initial model, which can introduce human bias, and involves multiple optimization processes to obtain the resistivity model, which is inconvenient.

In this section, we propose a regularized DL network to release the limitation of traditional DL inversion networks in guaranteeing the minimization of the data misfit. We introduce a multitask learning strategy (Asghar and Byun, 2021; Yoo et al., 2022) that combines a network performing forward modeling with the basic

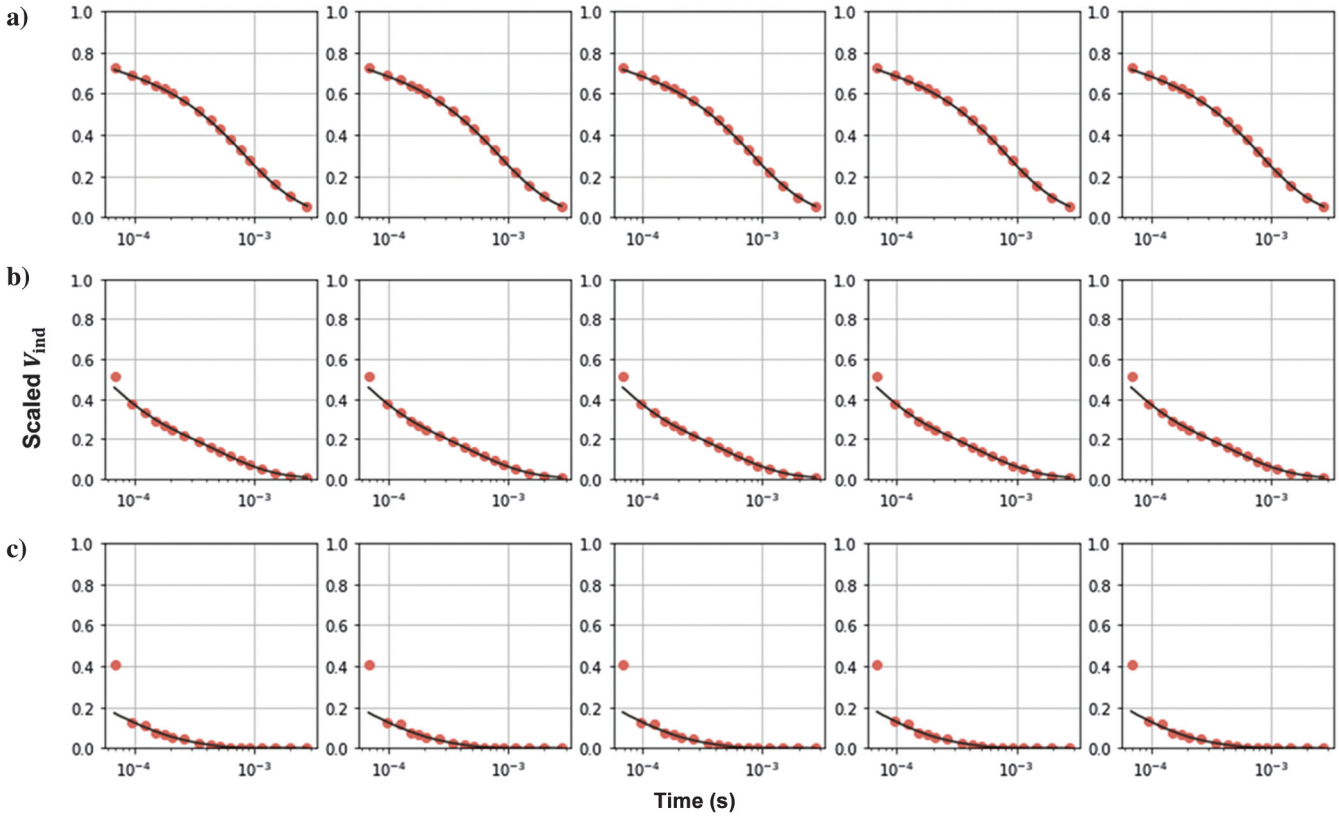

Figure 8. Interpolation results. The red dots represent the scaled raw data and the solid black line represents the data predicted by the interpolation network. First-channel raw data that exhibited especially large shifts are not input. The processed first channel is smoothly connected to the other channels.

inversion network. Our network contains two networks consisting of CNN-based ConvNeXt blocks to perform inversion and forward mapping, respectively.

ConvNeXt

ConvNeXt is a CNN-based neural network that also incorporates training techniques such as the Adam W optimizer (Loshchilov and Hutter, 2017), data augmentation (Zhong et al., 2017; Zhang et al., 2018; Yun et al., 2019), and regularization schemes including stochastic depth (Huang et al., 2016) and label smoothing. The design of the network, such as the patchify strategy (Liu et al., 2021), stage compute ratio (Radosavovic et al., 2019), and inverted bottleneck (Sandler et al., 2018) and large kernel size, also contribute to its superior performance. In addition, other strategies, such as depth-wise convolution (Chollet, 2017), are applied in this network. Although some of these strategies are not completely new, their collective use in ConvNeXt results in outstanding performance.

As shown in Figure 10, various techniques have been integrated into ConvNeXt. The "stage compute ratio" indicates how many ConvNeXt blocks are applied at each stage. Liu et al. (2022) adjust the number of blocks in each stage from (3, 4, 6, 3) in ResNet-50

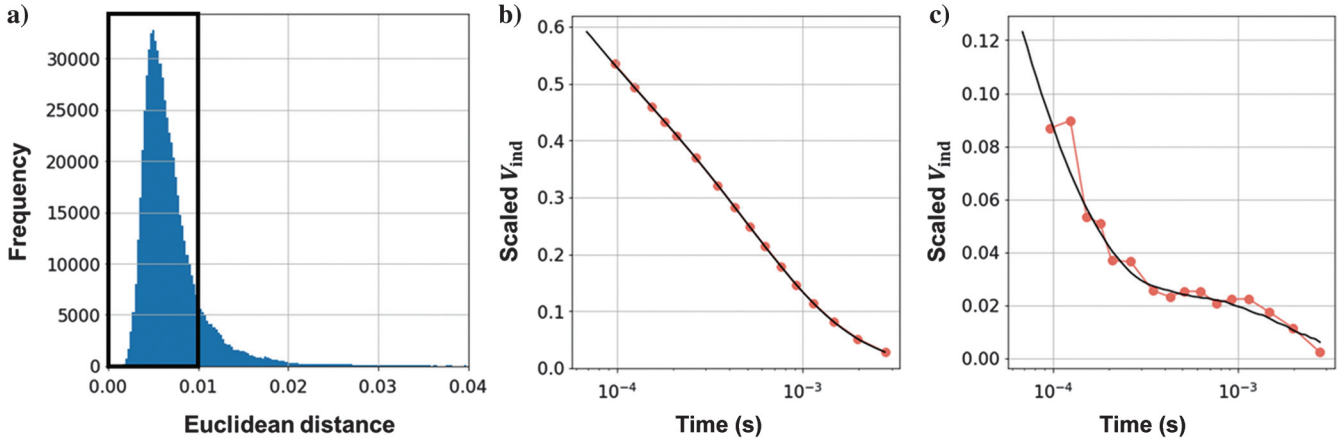

Figure 9. (a) Distribution of the calculated Euclidean distances. Most data are between 0 and 0.01 (within the black box). Example scaled voltage responses with Euclidean distances of (b) <0.01 and (c) >0.01. The red dots indicate the scaled raw data and the solid black line represents the data predicted by the interpolation network.

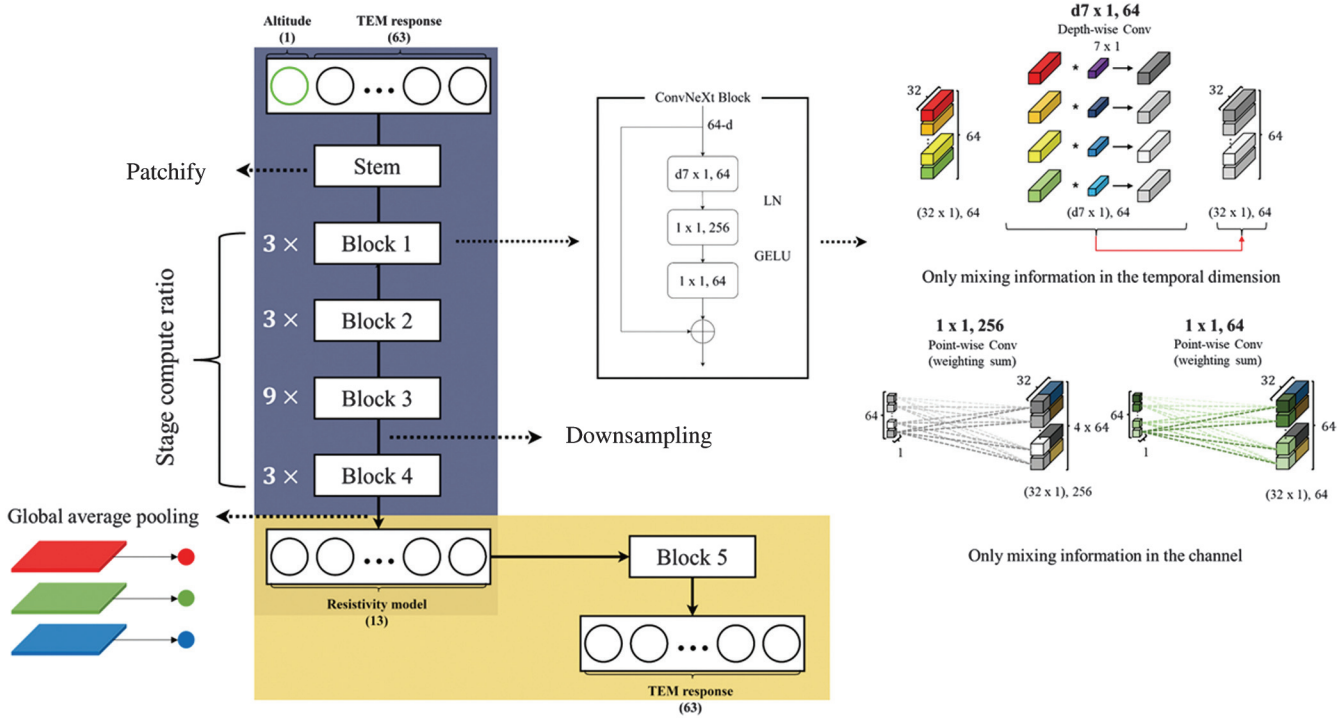

Figure 10. Schematic diagram of the developed inversion network with a regularization network consisting of ConvNeXt (Liu et al., 2022). The macro- and microdesigns are shown on the left and right, respectively.

(He et al., 2016), which is empirically determined, to (3, 3, 9, 3) in Swin-T (Liu et al., 2021), which improves the model accuracy. Depth-wise convolution is a special form of group convolution wherein the number of groups equals the number of channels. Group convolution is a strategy applied in ResNeXt (Xie et al., 2017) that separates convolution filters into multiple groups in the channel direction, which is popularized by MobileNet (Howard et al., 2017) and Xception (Chollet, 2017). It can greatly reduce the floating-point operations per second so that it prevents overfitting and improves the generalization ability. The inverted bottleneck refers to the fact that the hidden dimensions of the layers are wider than the input and output dimensions, i.e., the hidden dimensions are four times wider than the input. This idea is popularized by MobileNetV2 (Sandler et al., 2018). In this particular design, the depth-wise convolution layer is placed prior to the multilayer perceptron, which expands input dimensions by a factor of four, as does the Swin-T. Furthermore, ConvNeXt uses a large kernel to allow each layer to have a global receptive field (Liu et al., 2022).

Table 2. Detailed architecture of the modified ConvNeXt used to create the inversion network.

	ConvNeXt	Output size
Input	64	
Stem	(2, 64) stride 2	32
Block 1	$\begin{bmatrix} d7\times1, & 64 \\ 1\times1, & 256 \\ 1\times1, & 64 \end{bmatrix}\times3$	32
Block 2	$\begin{bmatrix} d7\times1, & 128 \\ 1\times1, & 512 \\ 1\times1, & 128 \end{bmatrix}\times3$	32
Block 3	$\begin{bmatrix} d7\times1, & 128 \\ 1\times1, & 512 \\ 1\times1, & 128 \end{bmatrix}\times9$	32
Block 4	$\begin{bmatrix} d7\times1, & 64 \\ 1\times1, & 256 \\ 1\times1, & 64 \end{bmatrix}\times3$	16
Output	13	

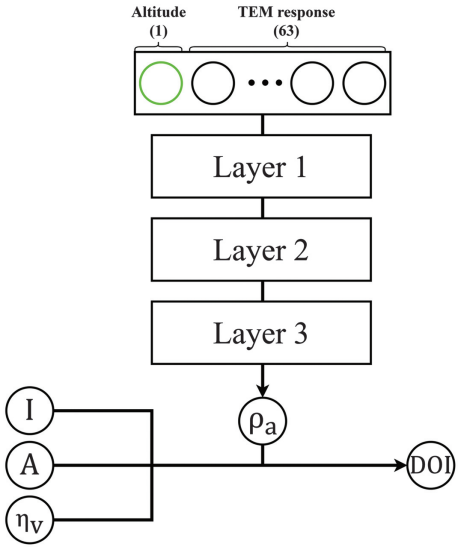

Figure 11. Schematic diagram of the DOI calculation process. The apparent resistivity is predicted by a simple neural network with three layers.

Model and regularization network

Traditional DL inversion studies have focused on minimizing the misfit of the resistivity models; however, this approach does not fundamentally ensure the fit to the data. To address this limitation and facilitate the incorporation of physics-based characteristics, we propose a combination of a regularization network and a model network, as shown in Figure 10. The cost function of the inversion network ($L_{\text{inversion}}$) consists of two distinct losses: one for the model network (L_{model}) and the other for the regularization network ($L_{\text{regularization}}$) as follows:

$$L_{\text{inversion}} = w_1' \cdot L_{\text{model}} + w_2' \cdot L_{\text{regularization}}, \tag{9}$$

where w_1' and w_2' represent the weights assigned to each loss function.

The blue box in Figure 10 shows the specifications for the model network of ConvNeXt blocks used in this study. We apply a nonoverlapping convolution of stride 2 and filter size 2 to the "stem," which performs downsampling of the 64 input datapoints

Table 3. Detailed architectures of the DOI network.

Layer	Type	Output shape
0	Input layer	64
1	Dense layer	256
2	Dense layer	128
3	Dense layer	64
4	Output layer	1

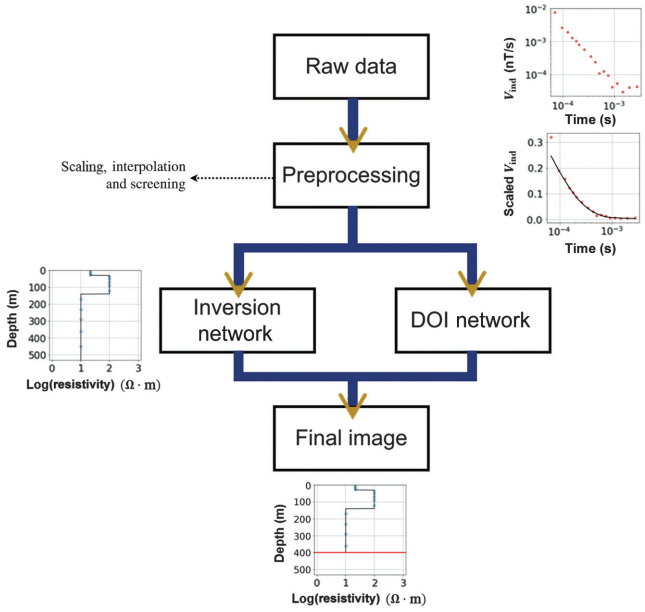

Figure 12. Schematic diagram of the proposed workflow from preprocessing to imaging.

(a min-max scaled altitude point + 63 interpolated datapoints) using an aggressive "patchify" method (Liu et al., 2022). The following four blocks are applied with a ratio of 1:1:3:1, but downsampling is confined to blocks 3 and 4 so that 16 datapoints are output before the "global averaging pooling." We opt for this pooling method rather than a fully connected layer to reduce computation costs. Using this pooling method, the network predicts the resistivity of 13 output nodes. Within the ConvNeXt block, we use layer normalization (LN) (Ba et al., 2016) as our regularization strategy, and we apply the Gaussian error linear unit (GELU) (Hendrycks and Gimpel, 2016) as the activation function. The parameters are summarized in Table 2. The loss for the model network (L_{model}) consists of the mean absolute error (MAE) and structural similarity index measure (SSIM) (Zhao et al., 2017) as follows:

$$L_{\text{model}}(m^p, m^l) = w_1 \cdot \text{MAE} + w_2 \cdot (1 - \text{SSIM}), \quad (10)$$

where m^p and m^l refer to the predicted and label resistivity models of the model network, respectively, and w_1 and w_2 are the weights assigned to each function. Here,

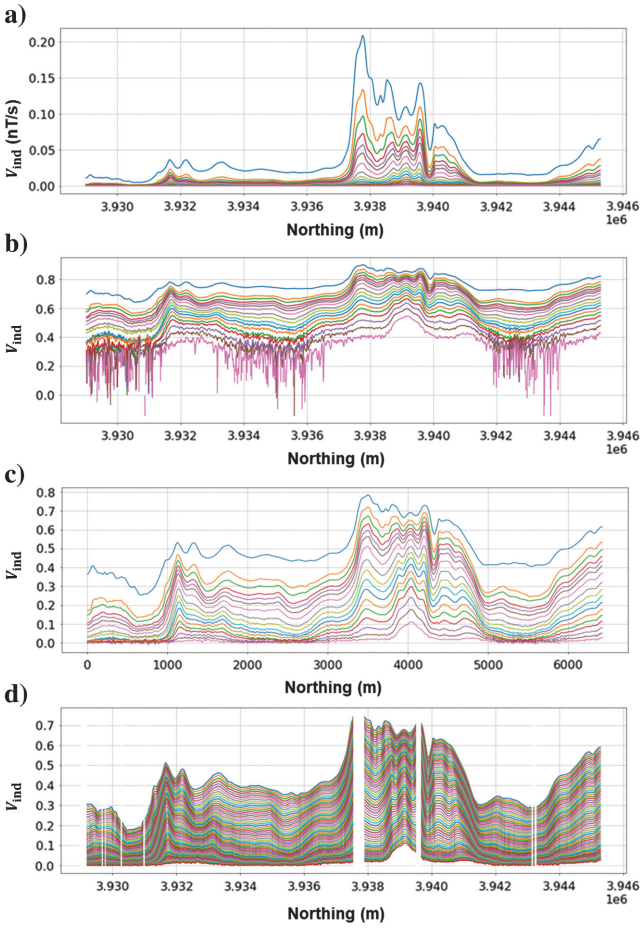

Figure 13. Induced voltage responses for the red survey line in Figure 3. (a) The induced voltage responses of the original 17 channels. (b and c) Min-max scaled responses obtained by logarithmic transformation and the shifted logarithmic transformation proposed in the present study, respectively. (d) Interpolated response by the interpolation network. The empty space represents the positions where data were excluded according to the altitude or Euclidean distance criteria.

$$\text{MAE}(m^p, m^l) = \frac{1}{M}\sum_{i=1}^{M} w_i^m \cdot |m^p(\theta, d_i) - m_i^l|, \quad (11)$$

where w^m denotes the weights for each layer of the resistivity model, M is the number of layers in the resistivity model, and θ corresponds to the model network's parameters. We introduce w^m to account for different sensitivities at each depth, as the sensitivity varies with depth:

$$\text{SSIM}(m^p, m^l) = \frac{(2\mu_p\mu_l + c_1)(2\sigma_{p,l} + c_2)}{(\mu_p^2 + \mu_l^2 + c_1)(\sigma_p^2 + \sigma_l^2 + c_2)}, \quad (12)$$

where c_1 and c_2 are small constants for numerical stability; μ_p and μ_l denote the mean value of the prediction and label, respectively; σ_p and σ_l represent the standard deviation values of the prediction and label, respectively; and $\sigma_{p,l}$ denotes the covariance between the prediction and label values. The SSIM evaluates the structural similarity between predicted data and label data, yielding a higher value when there is greater similarity between the two. By incorporating this term into our training process, we can adjust the network to minimize the "1-SSIM" value. This combined loss aims to minimize the model misfit while enhancing the structural similarity.

In addition to the model network, we introduce an additional block to regularize the model network, as indicated by the yellow box in Figure 10. The cost function of this network is defined as the MAE:

$$L_{\text{regularization}}(d^p, d^l) = \frac{1}{M}\sum_{i=1}^{M} |d^p(\theta^*, m_i) - d_i^l|, \quad (13)$$

where d^p and d^l refer to the predicted and label data of the regularization network, respectively, and θ^* corresponds to the regularization network's parameters. This loss aims to minimize the data misfit.

In this study, we assign values of 1 and 10 to w_1' and w_2' in equation 9, respectively, to equalize the contribution of each network. In addition, we determine values of 0.9 for w_1 and 0.1 for w_2 in equation 10 through a series of numerical tests.

DOI network

As shown in equation 5, the DOI is influenced by the magnetic moment, noise level, and ρ_a. The moment is usually measured during a survey, and the noise level can be obtained from measured data and the equipment. Thus, ρ_a is the only unknown. We construct a simple network that yielded ρ_a by identifying its relationship with the decay pattern of the secondary field. This network has three hidden layers and is trained using the generated responses and corresponding half-space resistivities. A total of 300 different half-space resistivity models are used to generate the training data set. Regularization involves 0.05 dropout. Here, "tanh" serves as the activation function and the L2-norm serves as the loss function. The prediction of ρ_a is shown in Figure 11. We calculate the DOI using the predicted ρ_a as well as the noise level and moment of field data. The detailed hyperparameters are provided in Table 3.

FIELD DATA APPLICATION

The entire workflow that produces the final resistivity model above the DOI using raw field data is shown in Figure 12. During preprocessing, severely noise-contaminated data are discarded, and

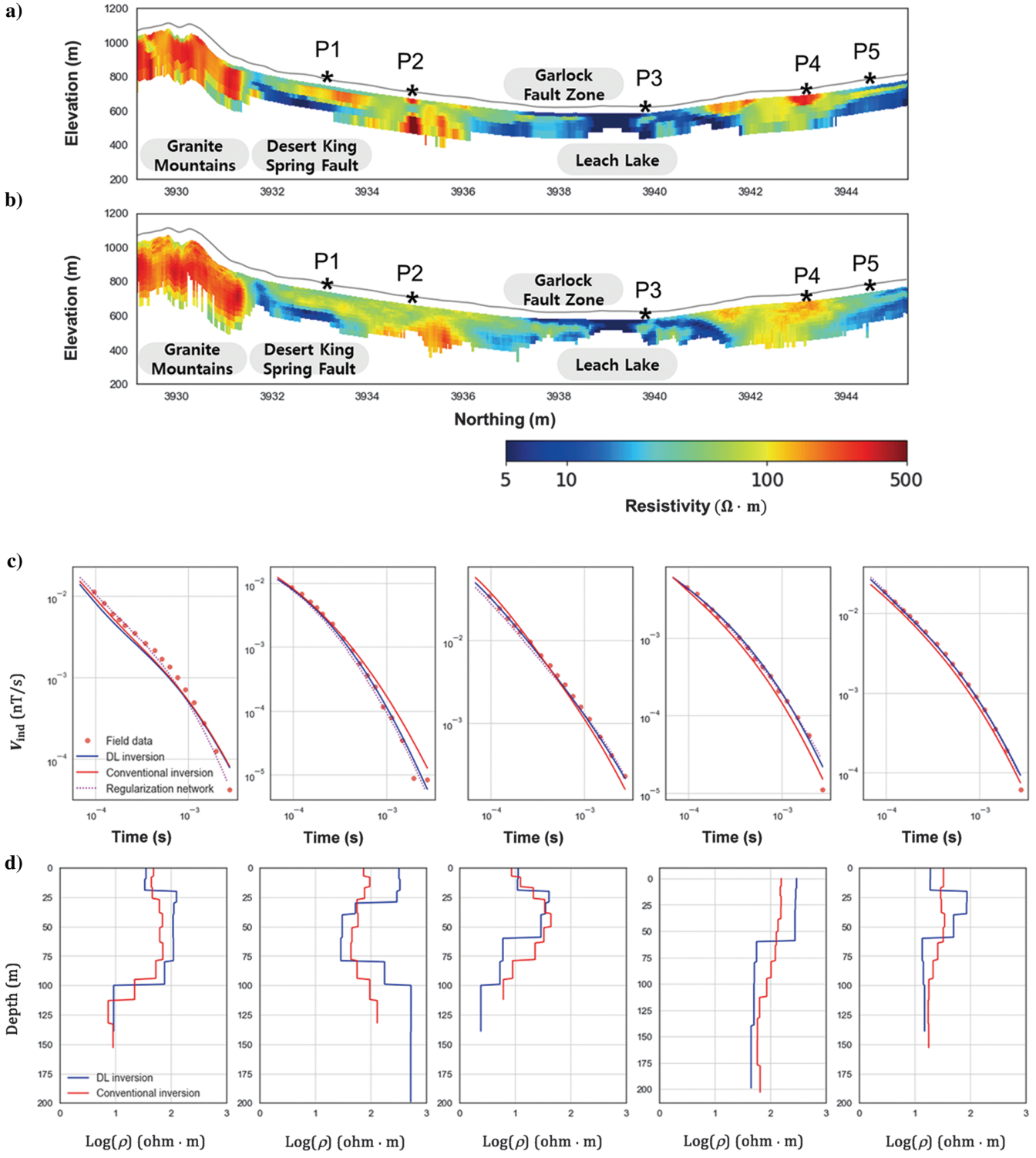

Figure 14. Inversion results above the DOI for the survey line marked in red in Figure 3. (a) A resistivity section inverted using our inversion workflow. (b) A resistivity section inverted using the conventional method (Bedrosian et al., 2014). (c) The voltage responses obtained from P1 to P5 are compared with the field data. The solid blue line indicates the voltage responses calculated from the predicted resistivity models by the DL network (the solid blue line shown in [d]), the solid red line indicates those from the inverted resistivity models by conventional inversion (the solid red line shown in [d]), and the dotted purple line indicates those predicted by the regularization network. (d) The resistivity models predicted by the conventional inversion method and the DL network at measurement points P1–P5.

the effects of noise are suppressed. Next, the resistivity model and DOI are predicted by two different networks, and the resistivity model above the DOI is finally displayed. To verify the performance of the workflow from preprocessing to imaging, we apply the workflow to an entire field data set. Before preprocessing, we exclude data that are highly sensitive to survey conditions or insensitive to subsurface resistivity. Thus, field data measured at altitudes of <20 m and >80 m are excluded.

The raw data from the red survey line in Figure 3 are shown in Figure 13a. If the 17-channel data are applied after applying min-max scaling using the general logarithmic transformation (see the aforementioned), the effect of noisy late-time data is exaggerated (Figure 14b). However, as shown in Figure 13c, the min-max scaling using the shifted logarithmic transformation of the induced voltages dramatically reduces the noise boost with the retention of the useful features of all channels. We use 10^{-3} as the epsilon, which is larger than the absolute minimum negative value (1.6×10^{-4}) of all field data. This new scaling approach allows for the successful interpolation of all 63 points by the preprocessing network (Figure 13d). The empty spaces in Figure 13d represent positions wherein data are excluded using the altitude or Euclidean distance criteria.

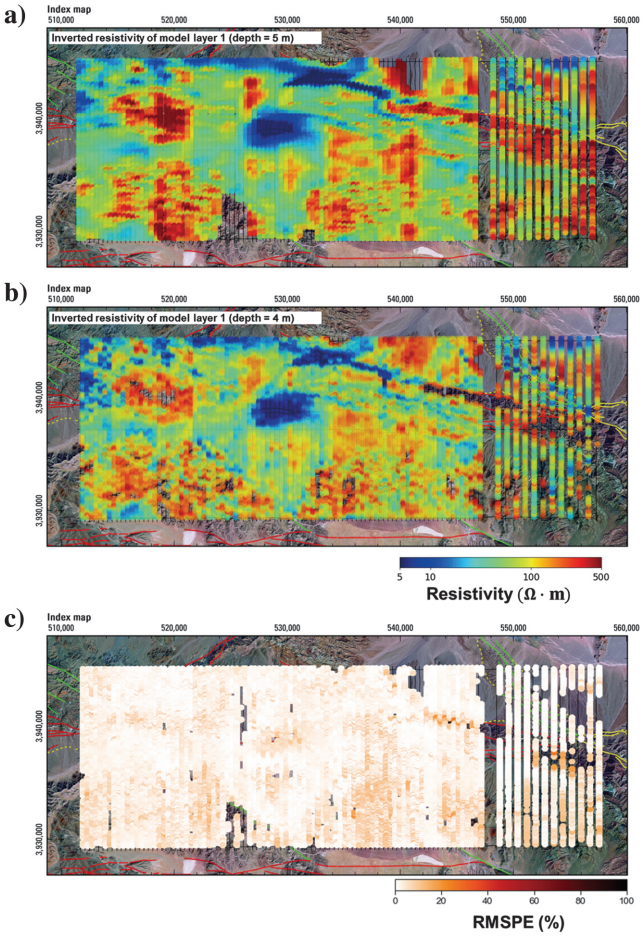

Figure 15. Depth-slice sections for the first inverted layer. (a) The DL-based results yielded by our workflow at a depth of 5 m overlaid on the geologic map of the USGS. (b) The conventional inversion result at a depth of 4 m (Bedrosian et al., 2014). (c) RMSPE error between the field data and the predicted field data overlaid on the map.

We use the preprocessed data to derive a resistivity model (via inversion) and the DOI. The inverted resistivity model above the DOI for the survey line is shown in Figure 14a. When we compare this with the conventional inversion of Figure 14b (Bedrosian et al., 2014), inverted using EM1DINV (Auken and Christiansen, 2004), the overall resistivity distributions are nearly identical, as are the locations of granitic mountains, faults, and lake. In addition, basin-bounding faults, such as the Desert King Fault and Spring Fault, are prominently shown by the contrast between the igneous rock and conductive sediments. However, the resistivity distribution as a function of depth sometimes differs from that of the conventional method (e.g., point P1 marked in Figure 14a and 14b). To validate our results, we simulate the induced voltage responses of the two 1D resistivity models predicted by the inversion network and conventional inversion method at P1. Then, we compare the two simulated datapoints to the field data. As shown in Figure 14c, the conventional model and our inversion network yield comparable decay curves; however, slight discrepancies are observed when compared with the field data. For clarity, we conduct simulations at P2, P3, P4, and P5. The conventional method and DL approach demonstrate a good fit with the field data; however, it is evident that the DL approach shows a more accurate prediction of the field data compared with conventional methods. Thus, it is clear that we encounter an instance of the "nonuniqueness problem" of 1D inversion. As shown in Figure 14d, the conventional inversion, aiming to address the nonuniqueness problem, incorporates smoothness constraints, resulting in a smoother resistivity model with respect to depth. In contrast, the resistivity variation obtained from the DL approach, trained on discrete models, exhibits more distinct boundaries, effectively highlighting the boundaries between different geologic units or structures.

Although we interpret the entire data set comprising 10,944,000 (684,000 × 16) datapoints, the complete analysis requires only 25 min using an Intel Core i9-10840X and a single NVIDIA GeForce RTX 3090 GPU. To validate the inversion results, a depth slice image of the first layer constructed using all survey lines (Figure 15a) is compared with that of Bedrosian et al. (2014) (Figure 15b). Given the differences in thickness of the first layer, Figure 16a and 16b shows the depth slice images from 5 and 4 m below the surface, respectively. However, this has little effect on the ATEM survey resolution. The conductive areas, granite basement, and faults displayed by our system agree with the conventionally obtained result. In addition, Figure 15c shows the root-mean-squared percentage errors (RMSPEs) between the field data and predicted data by the regularization network. The RMSPE is calculated by the following equation:

$$\mathrm{RMSPE} = \sqrt{\frac{1}{M}\sum\left(\frac{\log_{10} d_{\mathrm{field}} - \log_{10} d_{\mathrm{pred}}}{\log_{10} d_{\mathrm{field}}}\right)^2} \times 100, \quad (14)$$

where d_{field} is the measured data, d_{pred} is the predicted data by the regularization network, and M is the number of time channels. This error map serves as an indirect measure of the overall reliability of the inversion outcomes. The calculated average RMSPE of the entire field data is approximately 2%, indicating a low level of data misfit.

Figure 16 shows several depth slices over the entire survey area. As shown in Figure 16, not only is geologic connectivity according to the depth direction clearly delineated but also the DOI variation depending on the resistivity distribution of the upper layers is evidently identified.

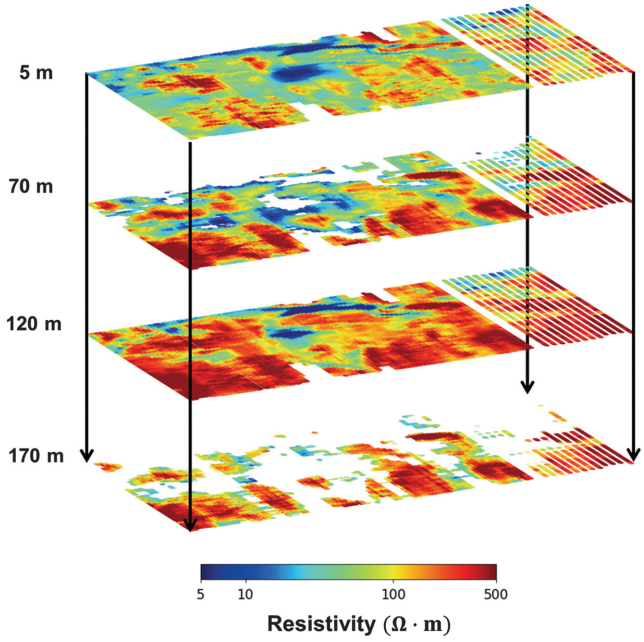

Figure 16. Depth-slice resistivity images of the entire survey area. Depth represents the distance from the surface.

CONCLUSION

This study presents an automated inversion workflow that covers all the steps from the preprocessing to the imaging of ATEM field data. Many researchers have focused on predicting reliable resistivities of the subsurface using DL techniques and they have achieved successful results to date. However, as EM inversion results are associated with different DOIs depending on the resistivity of the upper layers, reliable interpretation becomes impossible, especially at depth, when a DOI is not linked to the inversion result. In addition, for successful inversion of real ATEM field data, which can be heavily contaminated with noise, it is essential to discard improper data and suppress the effects of noise. Thus, we automate the entire workflow from preprocessing to imaging rather than developing only the inversion. In addition, during preprocessing, we shift the logarithmic transformation to suppress the noise in late-time channels and automatically discard severely distorted data using the Euclidean distance criteria. Furthermore, by incorporating a regularization network into the DL inversion network, we obtain reliable information on the predicted resistivity models, such as RMSPE between the field data and the predicted voltage response from these models, as well as more reasonable prediction results that guarantee the minimization of data misfit. However, this inversion process does not ensure smooth lateral transitions. This limitation should be considered in future work.

The proposed workflow is validated by applying it to the ATEM field data to understand and manage the groundwater resources of arid environments in the Leach Lake Basin (Fort Irwin, CA, USA) by the USGS. Although some of the resistivities predicted by DL inversion differed from the conventional results because the solutions of 1D inversions are nonunique, the distributions of igneous rocks, faults of Leach Lake, and King and Spring faults are well imaged using our system, as confirmed by comparisons with the conventional inversion and geologic survey.

In conclusion, we develop an overall workflow that includes the prediction of DOI and data misfit and preprocessing. The workflow is nearly automatic and very fast once the neural networks are trained and the results are highly accurate. We expect our system to aid the inversion of the ATEM survey data on the subsurface of large areas.

ACKNOWLEDGMENTS

This work was supported by a Korea CCUS Association (K-CCUS) grant from the Korean Government (MOE, MOTIE) (grant no. KCCUS20220001, Human Resources Program for Reduction of Greenhouse Gases) and the Reservoir Imaging with Seismic and EM Technology using Machine Learning (RISE.ML) Consortium at Hanyang University. The authors thank the USGS for sharing their airborne electromagnetic data on the Leach Lake Basin (Fort Irwin, CA, USA) and especially K. H. Lee for his constructive advice that greatly assisted our work.

DATA AND MATERIALS AVAILABILITY

Data associated with this research are confidential and cannot be released.

APPENDIX A

CALCULATION OF ATEM RESPONSES

The numerical modeling required to generate the training data set is performed using a modified EM1D algorithm (Kim et al., 1997), which is accurate and fast because it computes a semianalytic solution. Figure A-1 shows a schematic representation of the modeling workflow that generates the voltage responses of the AeroTEM IV system. First, forward modeling is conducted in the frequency domain using EM1D at 35 frequencies equally spaced on the logarithmic scale (from 1 Hz to 257 kHz) to calculate the time-domain responses.

Second, the frequency-domain responses are interpolated at 1 Hz intervals and the step-off responses are then derived using the discrete cosine transform (Newman et al., 1986):

$$B_{z,\mathrm{step}}(t) = -\frac{2\mu_0}{\pi}\int_0^\infty \frac{\mathrm{Im}[H_z(\omega)]}{\omega}\cos(\omega t)d\omega, \qquad \text{(A-1)}$$

where $\mathrm{Im}[H_z(\omega)]$ is the imaginary components of the vertical magnetic field in the frequency domain, μ_0 is the magnetic permeability of free space, and $B_{z,\mathrm{step}}(t)$ is the step-off response of the z-component.

Third, the magnetic B-fields induced by specific waveforms are calculated via a convolution procedure (Asten, 1987; Qi et al., 2019) based on the linear time invariant system theory:

$$B_z(t) = I(t) * B'_{z,\mathrm{step}}(t) = I'(t) * B_{z,\mathrm{step}}(t), \qquad \text{(A-2)}$$

where $B_z(t)$ is the vertical magnetic field stimulated by a specific waveform, $B'_{z,\mathrm{step}}(t)$ is the impulse response of the z-component, and $I'(t)$ is the derivative of the current waveform. Although both equations in equation A-2 are completely equivalent in theoretical terms, the latter provides more stable calculations because the error caused by any forward differences in the step-off responses can create major numerical problems during calculation. As the step-off re-

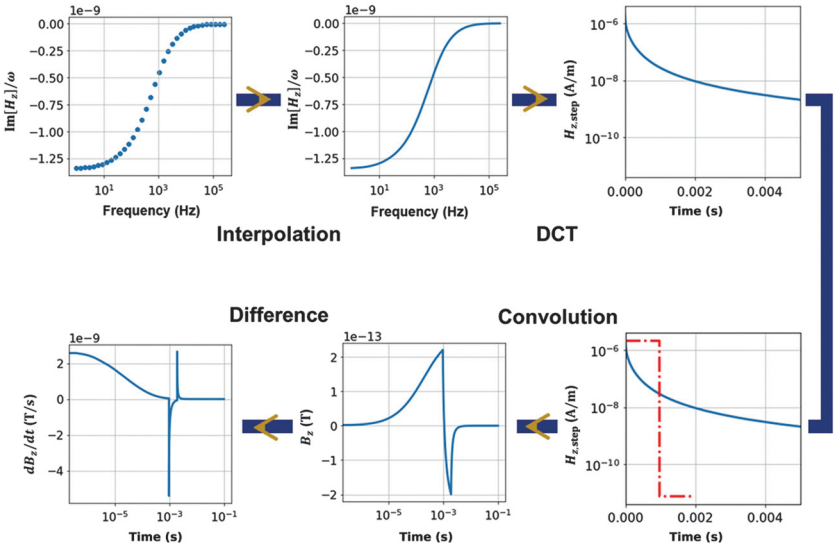

Figure A-1. Schematic representation of the AeroTEM modeling process. The derivative of the current waveform is superimposed on the step-off responses (the dashed-dotted red line).

sponses are derived by summing the cosine waves, cosine differences may be unstable and imprecise, especially at high frequencies.

Fourth, to calculate the voltage responses, we approximate the differentiation by discretizing the magnetic B-fields obtained in equation A-2. This discretization is achieved using the forward difference method as

$$V_{\text{ind}} = \frac{d}{dt} B_z(t), \tag{A-3}$$

where V_{ind} is the induced voltage response.

Finally, downsampling to 63 datapoints from 2.14 to 4.71 ms using the densely simulated data from 10^{-5} to 5×10^{2} ms yields the input data for training.

REFERENCES

Asghar, S., and J. Byun, 2021, Semisupervised facies classification with reconstruction cooperation: First International Meeting for Applied Geoscience & Energy, SEG, Expanded Abstracts, 2173–2177, doi: 10.1190/segam2021-3594315.1.

Asif, M. R., P. K. Maurya, N. Foged, J. J. Larsen, E. Auken, and A. V. Christiansen, 2022, Automated transient electromagnetic data processing for ground-based and airborne systems by a deep learning expert system: IEEE Transactions on Geoscience and Remote Sensing, **60**, 1–14, doi: 10.1109/TGRS.2022.3202304.

Asten, M. W., 1987, Full transmitter waveform transient electromagnetic modeling and inversion for soundings over coal measures: Geophysics, **52**, 279–288, doi: 10.1190/1.1442302.

Auken, E., and A. V. Christiansen, 2004, Layered and laterally constrained 2D inversion of resistivity data: Geophysics, **69**, 752–761, doi: 10.1190/1.1759461.

Auken, E., A. V. Christiansen, B. H. Jacobsen, N. Foged, and K. I. Sørensen, 2005, Piecewise 1D laterally constrained inversion of resistivity data: Geophysical Prospecting, **53**, 497–506, doi: 10.1111/j.1365-2478.2005.00486.x.

Auken, E., A. V. Christiansen, J. H. Westergaard, C. Kirkegaard, N. Foged, and A. Viezzoli, 2009, An integrated processing scheme for high-resolution airborne electromagnetic surveys, the SkyTEM system: Exploration Geophysics, **40**, 184–192, doi: 10.1071/EG08128.

Ba, J. L., J. R. Kiros, and G. E. Hinton, 2016, Layer normalization: arXiv preprint, doi: 10.48550/arXiv.1607.06450.

Bai, P., G. Vignoli, A. Viezzoli, J. Nevalainen, and G. Vacca, 2020, (Quasi-) real-time inversion of airborne time-domain electromagnetic data via artificial neural network: Remote Sensing, **12**, 3440, doi: 10.3390/rs12203440.

Bang, M., J. Byun, and S. J. Seol, 2022, Deep neural network-based airborne EM data inversion suitable for mountainous field sites: 84th Annual International Conference and Exhibition, EAGE, Extended Abstracts, doi: 10.3997/2214-4609.202210341.

Bedrosian, P. A., L. B. Ball, and B. R. Bloss, 2014, Airborne electromagnetic data and processing within Leach Lake Basin, Fort Irwin, California, *in* D. C. Buesch, ed., Geology and geophysics applied to groundwater hydrology at Fort Irwin, California: U.S. Geological Survey Open File Report 2013-1024, 20.

Chen, K., X. Pu, Y. Ren, H. Qiu, F. Lin, and S. Zhang, 2022, TEMDnet: A novel deep denoising network for transient electromagnetic signal with signal-to-image transformation: IEEE Transactions on Geoscience and Remote Sensing, **60**, 1–18, doi: 10.1109/tgrs.2020.3034752.

Chollet, F., 2017, Xception: Deep learning with depthwise separable convolutions: IEEE Conference on Computer Vision and Pattern Recognition, 1800–1807.

Christensen, N. B., 2002, A generic 1-D imaging method for transient electromagnetic data: Geophysics, **67**, 438–447, doi: 10.1190/1.1468603.

Christiansen, A. V., and E. Auken, 2010, A global measure for depth of investigation in EM and DC modeling: ASEG2010, 21st Geophysical Conference, Extended Abstracts, 1–4, doi: 10.1081/22020586.2010.12042021.

Colombo, D., E. Turkoglu, W. Li, E. Sandoval-Curiel, and D. Rovetta, 2021, Physics-driven deep-learning inversion with application to transient electromagnetics: Geophysics, **86**, no. 3, E209–E224, doi: 10.1190/geo2020-0760.1.

Cox, L. H., G. A. Wilson, and M. S. Zhdanov, 2010, 3D inversion of airborne electromagnetic data using a moving footprint: Exploration Geophysics, **41**, 250–259, doi: 10.1071/EG10003.

Dethlefsen, F., R. Köber, D. Schäfer, S. A. A. Hagrey, G. Hornbruch, M. Ebert, M. Beyer, J. Großmann, and A. Dahmke, 2013, Monitoring approaches for detecting and evaluating CO_2 and formation water leakages into near-surface aquifers: Energy Procedia, **37**, 4886–4893, doi: 10.1016/j.egypro.2013.06.399.

Feng, B., J. Zhang, D. Li, and Y. Bai, 2020, Resistivity-depth imaging with the airborne transient electromagnetic method based on an artificial neural network: Journal of Environmental and Engineering Geophysics, **25**, 355–368, doi: 10.32389/JEEG19-087.

Google Earth, 2014, Leach Lake Basin, Fort Irwin, California, USA, 35°34′38 N116°37′01W, http://www.earth.google.com, accessed 28 November 2022.

Guillemoteau, J., P. Sailhac, and M. Behaegel, 2012, Fast 2D inversion of airborne transient electromagnetic data: A synthetic case: Near Surface Geoscience 2012, 1st EAGE/GRSG Remote Sensing Workshop, cp-305-00015, doi: 10.3997/2214-4609.20143290.

Hauser, J., J. Gunning, and D. Annetts, 2015, Probabilistic inversion of airborne electromagnetic data under spatial constraints: Geophysics, **80**, no. 2, E135–E146, doi: 10.1190/geo2014-0389.1.

He, K., X. Zhang, S. Ren, and J. Sun, 2016, Identity mappings in deep residual networks, *in* B. Leibe, J. Matas, N. Sebe, and M. Welling, eds., European Conference on Computer Vision: Springer International Publishing, 630–645.

Hendrycks, D., and K. Gimpel, 2016, Gaussian error linear units (GELUs): arXiv preprint, doi: 10.48550/arXiv.1606.08415.

Howard, A. G., M. Zhu, B. Chen, D. Kalenichenko, W. Wang, T. Weyand, M. Andreetto, and H. Adam, 2017, MobileNets: Efficient convolutional neural networks for mobile vision applications: arXiv preprint, doi: 10.48550/arXiv.1704.04861.

Huang, G., Y. Sun, Z. Liu, D. Sedra, and K. Q. Weinberger, 2016, Deep networks with stochastic depth, *in* B. Leibe, J. Matas, N. Sebe, and M. Welling, eds., European Conference on Computer Vision: Springer International Publishing, 646–661.

Huang, H., and J. Rudd, 2008, Conductivity-depth imaging of helicopter-borne TEM data based on a pseudolayer half-space model: Geophysics, **73**, no. 3, F115–F120, doi: 10.1190/1.2904984.

Hutchinson, D., D. K. Hutchinson, I. C. Roach, and M. T. Costelloe, 2010, Depth of investigation grid for regional airborne electromagnetic surveys: Preview, **145**, 38–39.

Kang, S., N. Dewar, and R. Knight, 2021, The effect of power lines on time-domain airborne electromagnetic data: Geophysics, **86**, no. 2, E123–E141, doi: 10.1190/geo2020-0089.1.

Kang, S., D. Fournier, and D. W. Oldenburg, 2017, Inversion of airborne geophysics over the DO-27/DO-18 kimberlites — Part 3: Induced polarization: Interpretation, **5**, no. 3, T327–T340, doi: 10.1190/INT-2016-0141.1.

Kang, S., and D. W. Oldenburg, 2016, On recovering distributed IP information from inductive source time domain electromagnetic data: Geophysical Journal International, **207**, 174–196, doi: 10.1093/gji/ggw256.
Kim, H. J., Y. Song, and K. H. Lee, 1997, High-frequency electromagnetic inversion for a dispersive layered earth: Journal of Geomagnetism and Geoelectricity, **49**, 1439–1450, doi: 10.5636/jgg.49.1439.
Kirsch, R., 2009, Groundwater geophysics: A tool for hydrogeology: Springer.
Law, D., K. A. Mohd Noh, and A. G. Md Rafek, 2019, Application of transient electromagnetic (TEM) method for delineation of mineralized fracture zones: IOP Conference Series: Earth and Environmental Science, **279**, 012038, doi: 10.1088/1755-1315/279/1/012038.
Li, J., Y. Liu, C. Yin, X. Ren, and Y. Su, 2020, Fast imaging of time-domain airborne EM data using deep learning technology: Geophysics, **85**, no. 5, E163–E170, doi: 10.1190/geo2019-0015.1.
Li, R., H. Zhang, S. Gao, Z. Wu, and C. Guo, 2021, An improved extreme learning machine algorithm for transient electromagnetic nonlinear inversion: Computers & Geosciences, **156**, 104877, doi: 10.1016/j.cageo.2021.104877.
Liu, G., and M. Asten, 1993, Conductance-depth imaging of airborne TEM data: Exploration Geophysics, **24**, 655–661, doi: 10.1071/EG993655.
Liu, Z., Y. Lin, Y. Cao, H. Hu, Y. Wei, Z. Zhang, S. Lin, and B. Guo, 2021, Swin transformer: Hierarchical vision transformer using shifted windows: IEEE/CVF International Conference on Computer Vision, 9992–10002.
Liu, Z., H. Mao, C.-Y. Wu, C. Feichtenhofer, T. Darrell, and S. Xie, 2022, A ConvNet for the 2020s: Proceedings of the IEEE/CVF Conference on Computer Vision and Pattern Recognition, 11976–11986.
Loshchilov, I., and F. Hutter, 2017, Decoupled weight decay regularization: arXiv preprint, doi: 10.48550/arXiv.1711.05101.
Madsen, L. M., T. Bording, D. Grombacher, N. Foged, N. Foley, H. A. Dugan, P. T. Doran, J. Mikucki, S. Tulaczyk, and E. Auken, 2022, Comparison of ground-based and airborne transient electromagnetic methods for mapping glacial and permafrost environments: Cases from McMurdo Dry Valleys, Antarctica: Cold Regions Science and Technology, **199**, 103578, doi: 10.1016/j.coldregions.2022.103578.
Newman, G. A., G. W. Hohmann, and W. L. Anderson, 1986, Transient electromagnetic response of a three-dimensional body in a layered earth: Geophysics, **51**, 1608–1627, doi: 10.1190/1.1442212.
Pfaffhuber, A. A., S. Monstad, and J. Rudd, 2009, Airborne electromagnetic hydrocarbon mapping in Mozambique: Exploration Geophysics, **40**, 237–245, doi: 10.1071/EG09011.
Puzyrev, V., and A. Swidinsky, 2021, Inversion of 1D frequency- and time-domain electromagnetic data with convolutional neural networks: Computers & Geosciences, **149**, 104681, doi: 10.1016/j.cageo.2020.104681.
Qi, Y., L. Huang, X. Wu, W. Zhu, G. Fang, and G. Yu, 2019, Full waveform modeling of transient electromagnetic response based on temporal interpolation and convolution method: Pure and Applied Geophysics, **176**, 2465–2477, doi: 10.1007/s00024-017-1627-6.
Radosavovic, I., J. Johnson, S. Xie, W.-Y. Lo, and P. Dollar, 2019, On network design spaces for visual recognition: IEEE/CVF International Conference on Computer Vision, 1882–1890.
Sandler, M., A. Howard, M. Zhu, A. Zhmoginov, and L.-C. Chen, 2018, MobileNetV2: Inverted residuals and linear bottlenecks: IEEE/CVF Conference on Computer Vision and Pattern Recognition, 4510–4520.
Smith, R. S., M. D. O'Connell, and L. H. Poulsen, 2004, Using airborne electromagnetics surveys to investigate the hydrogeology of an area near Nyborg, Denmark: Near Surface Geophysics, **2**, 123–130, doi: 10.3997/1873-0604.2004009.
Spies, B. R., 1989, Depth of investigation in electromagnetic sounding methods: Geophysics, **54**, 872–888, doi: 10.1190/1.1442716.
Tartaras, E., M. S. Zhdanov, K. Wada, A. Saito, and T. Hara, 2000, Fast imaging of TDEM data based on S-inversion: Journal of Applied Geophysics, **43**, 15–32, doi: 10.1016/S0926-9851(99)00030-0.
USGS, 2011, Report on a helicopter-borne AeroTEM system electromagnetic and magnetic survey Leach Basin Fort Irwin Army Base Aeroquest International, https://pubs.usgs.gov/of/2013/1024/g/downloads/ofr2013-1024-g_appendix_a.pdf, accessed 16 January 2024.
Viezzoli, A., A. V. Christiansen, E. Auken, and K. Sørensen, 2008, Quasi-3D modeling of airborne TEM data by spatially constrained inversion: Geophysics, **73**, no. 3, F105–F113, doi: 10.1190/1.2895521.
Ward, S. H., and G. W. Hohmann, 1988, 4. Electromagnetic theory for geophysical applications, *in* M. N. Nabighian, ed., Electromagnetic methods in applied geophysics: Volume 1, Theory. Investigations in geophysics: SEG, 130–311.
Weidelt, P., 1982, Response characteristics of coincident loop transient electromagnetic systems: Geophysics, **47**, 1325–1330, doi: 10.1190/1.1441393.
Wu, S., Q. Huang, and L. Zhao, 2021a, Convolutional neural network inversion of airborne transient electromagnetic data: Geophysical Prospecting, **69**, 1761–1772, doi: 10.1111/1365-2478.13136.
Wu, S., Q. Huang, and L. Zhao, 2021b, De-noising of transient electromagnetic data based on the long short-term memory-autoencoder: Geophysical Journal International, **224**, 669–681, doi: 10.1093/gji/ggaa424.
Wu, S., Q. Huang, and L. Zhao, 2022, Instantaneous inversion of airborne electromagnetic data based on deep learning: Geophysical Research Letters, **49**, e2021GL097165, doi: 10.1029/2021GL097165.
Xie, S., R. Girshick, P. Dollar, Z. Tu, and K. He, 2017, Aggregated residual transformations for deep neural networks: IEEE Conference on Computer Vision and Pattern Recognition, 5987–5995.
Yang, D., and D. W. Oldenburg, 2013, 3D conductivity models of Lalor Lake VMS deposit from ground loop and airborne EM data sets: ASEG 2013-23rd Geophysical Conference, Extended Abstracts, 1–4, doi: 10.1071/ASEG2013ab296.
Yoo, J., D. Kim, J. Choi, and J. Byun, 2022, Impedance inversion based on domain adaptation technique with reconstruction: IEEE Geoscience and Remote Sensing Letters, **19**, 1–5, doi: 10.1109/LGRS.2022.3179492.
Yun, S., D. Han, S. Chun, S. J. Oh, Y. Yoo, and J. Choe, 2019, CutMix: Regularization strategy to train strong classifiers with localizable features: IEEE/CVF International Conference on Computer Vision, 6022–6031.
Zhang, H., M. Cisse, Y. N. Dauphin, and D. Lopez-Paz, 2018, mixup: Beyond empirical risk minimization: arXiv preprint, doi: 10.48550/arXiv.1710.09412.
Zhao, H., O. Gallo, I. Frosio, and J. Kautz, 2017, Loss functions for image restoration with neural networks: IEEE Transactions on Computational Imaging, **3**, 47–57, doi: 10.1109/TCI.2016.2644865.
Zhong, Z., L. Zheng, G. Kang, S. Li, and Y. Yang, 2017, Random erasing data augmentation: Proceedings of the AAAI Conference on Artificial Intelligence, 34, 13001–13008.

Biographies and photographs of the authors are not available.